

Modeling propagation in shallow water with the range-dependent sea surfaces and fluid seabeds using the equivalent source method

Tengjiao He,^{a)} Shiqi Mo,^{b)} Wei Guo,^{a)} and Erzheng Fang^{a)}

College of Underwater Acoustic Engineering, Harbin Engineering University, Harbin 150001, China

ABSTRACT:

This paper describes a shallow water range-dependent propagation model (RPM) based on the equivalent source method (ESM). The proposed model allows both the sea surface and fluid seabed to vary with the propagation range. The proposed equivalent source method-based range-dependent propagation model (ESM-RPM) utilizes three sets of equivalent sources, placed above the sea surface, below the seabed, and above the seabed, which replace the sea surface reflection, seabed reflection, and seabed transmission, respectively. The unknown strengths of the equivalent sources can be determined by solving an inverse problem based on the boundary conditions. The capability of the ESM-RPM for propagation in refractive water is demonstrated by evaluating the Green's function using a modal projection method. Numerical simulations are conducted in iso-velocity and refractive shallow water with an underwater canyon and corrugated surface waves, including two-dimensional (2-D) propagation across the canyon and three-dimensional (3-D) propagation along the canyon. Further simulations demonstrate the 2-D across-canyon and 3-D along-canyon propagations with random rough sea surfaces. The results show that the proposed ESM-RPM provides efficient, benchmark-quality numerical solutions that accurately capture the mode coupling associated with the varying cross section of the waveguide. Thus, the model has great potential to be applied in benchmarking propagation in shallow water with the varying sea surface and seabed. © 2021 Acoustical Society of America.

<https://doi.org/10.1121/10.0003385>

(Received 2 September 2020; revised 29 December 2020; accepted 6 January 2021; published online 9 February 2021)

[Editor: Nicholas P. Chotiros]

Pages: 997–1011

I. INTRODUCTION

The modeling of propagation in shallow water has received considerable interest because it is crucial to underwater communication, localization, and navigation. Classical theories, such as normal mode (Pekeris, 1948) and wavenumber integral approaches (DiNapoli and Deavenport, 1980), have been developed to deal with propagation in idealized shallow water with parallel boundaries. The boundaries of the real ocean, however, are range dependent or even time dependent, for instance, varying seabeds induced by changes in continental shelf topography or moving rough sea surfaces driven by the wind force. Mode-coupling effects associated with the varying cross section of the waveguide have a significant impact on the sound propagation in such complex environments, especially in the presence of the sound speed profile (SSP), preventing classical theories from being used directly. Therefore, an appropriate model, which is capable of accurately capturing the mode coupling, is required to calculate the sound propagation in such complex environments.

Coupled mode (CM) theory (Evans, 1983; Fawcett, 1992; McDonald, 1996) has been widely used to solve range-dependent propagation problems. The basic idea of the CM is to divide the range-dependent waveguide into several range-independent local sections so that the field can be separated in terms of local modes and their range-dependent amplitudes. By satisfying the continuity of pressure and normal particle velocity on the boundary between each local section, the mode amplitudes can be solved globally. The CM can be further extended to calculate three-dimensional (3-D) propagation by incorporating the horizontal refraction equation (Ballard, 2013; Ballard *et al.*, 2015). However, when dealing with high-frequency or suddenly changing environments, the CM requires a large number of modes or local sections to obtain good convergence, which tends to intensify the computational load. Additionally, the number of modes taken into account should be treated very carefully when mode cutoff occurs. Another applicable technique for range-dependent propagation is the parabolic equation (PE; Tappert, 1977), which has been extensively used in underwater acoustics over the past two decades. The technique uses a parabolic approximation to the Helmholtz equation, and then retains only the outgoing wave component. Such a one-way solution provided by the PE technique is numerically efficient, making it suitable for calculating 3-D scenarios (Lin *et al.*, 2013;

^{a)}Also at: Key Laboratory of Marine Information Acquisition and Security, Harbin Engineering University, Ministry of Industry and Information Technology, Harbin 150001, China.

^{b)}Electronic mail: moshqiqi@hrbeu.edu.cn

Sturm, 2016). However, the inherent phase errors in the approximations restrict the angular range around the dominant propagation direction. Further numerical effort is required to obtain more wide-angled PE approximations (Collins, 1989, 1993).

In recent years, there has been increasing use of the finite element method (FEM) in underwater acoustics (Isakson and Chotiros, 2011, 2014; Isakson *et al.*, 2014; Simon *et al.*, 2018). The advantage of the FEM is its applicability for arbitrary environments and ranges as it is customizable and based on the Helmholtz equation without any approximations. Hence, the FEM can be considered as the benchmark for range-dependent propagation. Nevertheless, the FEM is cumbersome because of its meshing requirements, especially for the Monte Carlo simulations required by studies related to rough scattering from boundaries. Furthermore, the computational load rapidly increases as the frequency increases. Several pieces of literature have demonstrated the capability of the spectral element method (SEM) for the underwater acoustic propagation in the time-domain (Cristini and Komatitsch, 2012; Bottero *et al.*, 2016; Bottero *et al.*, 2018). The SEM is based on a high-order piecewise polynomial approximation of the weak formulation of the wave equation, providing a numerically efficient full-wave solution of the wavefield. Nevertheless, the SEM still relies on meshing that may restrict the size of the problem. Readers can find a more comprehensive review of the modeling of underwater acoustic propagation in the book written by Jensen *et al.* (2011).

Apart from the above models, the capability of the equivalent source method (ESM; Koopmann *et al.*, 1989) for propagation in shallow water with the varying seabed (Abawi and Porter, 2007) or sea surface (He *et al.*, 2020) has been demonstrated. Initially, the ESM was developed to calculate the field radiated from a complex radiator with the basic idea of replacing the radiated field with a superposition of fields generated by a set of equivalent sources within the radiator. Equivalent sources are offset from their corresponding boundaries, and their strengths can be solved by satisfying the boundary condition at the surface of the radiator. Therefore, the ESM can circumvent the inherent singularities problem in the boundary element method (BEM), and its numerical implementation is simple because the bases are nodes rather than elements. Compared with the FEM, the ESM-based models solve the boundary integral problem instead of the whole physical domain and are, therefore, more numerically efficient. Moreover, the ESM-based models are, in theory, as accurate as the FEM. Such a model provides a full-wave solution for the wavefield in shallow water with a varying cross section. To the best of our knowledge, no ESM-based propagation model in shallow water with both the varying sea surface and fluid seabed has been developed yet. Moreover, none of the ESM-based propagation models has taken sound speed variation into account. The goals of this paper are to bridge these two gaps and provide a benchmark-quality and numerically efficient

solution that is capable of accurately capturing the mode-coupling induced by varying boundaries.

This paper proposes an equivalent source method-based range-dependent propagation model (ESM-RPM) that allows both the sea surface and fluid seabed to vary with the propagation range. In the ESM-RPM, three sets of equivalent sources with unknown strengths are placed above the sea surface, below the seabed, and above the seabed to replace the sea surface reflection, seabed reflection, and seabed transmission, respectively. For a given incident field, the unknown source strengths can be solved by satisfying the pressure-release condition and continuity of pressure and normal displacement on the sea surface and seabed. After determining the source strengths, fields at arbitrary positions can be solved. To extend the ESM-RPM to refractive water, the Green's function for refractive water is evaluated using a modal projection method, incorporating the perfectly matched layers (PMLs) technique (Bérenger 1994). The mode of the field in a refractive free-space truncated by two PMLs is projected onto basic orthogonal modes of the field in a waveguide bounded by the two outer boundaries of the PMLs. Such a modal projection yields a generalized matrix eigenvalue problem through which the modal eigenvalues and eigenvectors can be solved. Numerical simulations are first presented in shallow water with an underwater canyon and corrugated surface waves. The model is validated by comparisons with a finite element (FE) model. The sound field separation enabled by the ESM-RPM is applied to provide insights into the scattering and refractive effects. To demonstrate the effects of out-of-plane scattering, a cosine transform of an assembly of 2-D fields is then performed to calculate the 3-D propagation in the horizontal plane along the canyon. Finally, both the 2-D across-canyon and 3-D along-canyon propagations are calculated with random rough sea surfaces to show the versatility of the ESM-RPM for demonstrating the effects of scattering from random rough sea surfaces. The remainder of this paper is organized as follows. Section II describes the formulation of the ESM-RPM, and Sec. III presents numerical results and discussion. Finally, the conclusions to this study are summarized in Sec. IV.

II. METHOD

A. The 2-D ESM-based propagation model with the varying sea surface and seabed

As shown in Fig. 1, consider the range-dependent shallow water with a sound speed and density of c_w and ρ_w in the water column, respectively, and c_s and ρ_s in the seabed, respectively. The subscripts w and s specify the water and seabed layers, respectively. The Helmholtz equation governing the 2-D sound field $p(\mathbf{r})$ in the waveguide is given by

$$[\nabla^2 + k^2]p(\mathbf{r}) = 0, \quad (1)$$

where $\mathbf{r} = (x, z)$ is the position vector, and k is the wave-number that becomes $k_w = \omega/c_w$ in water and $k_s = \omega/c_s$ in the seabed, and ω is the angular frequency. The pressure-release boundary condition at the sea surface and the

continuity of pressure and displacement across the water/seabed interface can be expressed as

$$\begin{cases} p(\mathbf{r}_a) = 0, \\ p(\mathbf{r}_b)_- = p(\mathbf{r}_b)_+, \\ u(\mathbf{r}_b)_- = u(\mathbf{r}_b)_+, \end{cases} \quad (2)$$

where r_a and r_b are the positions of the sea surface and seabed boundary, respectively, and u is the normal displacement at the water/seabed interface.

Then, consider the Helmholtz equation for a line source

$$[\nabla^2 + k^2]G(\mathbf{r}, \mathbf{r}'|k) = \delta(\mathbf{r} - \mathbf{r}'), \quad (3)$$

where $G(\mathbf{r}, \mathbf{r}'|k)$, the Green's function at \mathbf{r} due to the source at \mathbf{r}' , is given by

$$\begin{cases} G^{sp}(\mathbf{r}, \mathbf{r}'|k) = \frac{i}{4}H_0^{(1)}(k|\mathbf{r} - \mathbf{r}'|), \\ G^u(\mathbf{r}, \mathbf{r}'|k) = \frac{1}{\rho\omega^2} \hat{\mathbf{n}} \nabla G^{sp}(\mathbf{r}, \mathbf{r}'|k), \end{cases} \quad (4)$$

where the superscripts sp and u indicate that G^{sp} and G^u are the pressure and normal displacement Green's function, respectively, $\hat{\mathbf{n}}$ represents the unit normal vector to the boundary, and $H_0^{(1)}$ is the first-class Hankel function of order zero. For the normal displacement Green's function, the subscript of ρ will change accordingly with that of k . The Green's function is a fundamental solution of Eq. (3), automatically satisfying the Sommerfeld radiation condition. Because the basis functions given by Eq. (4) satisfy Eq. (1), the solution of Eq. (1) can be constructed by the superposition of the basis functions. The ESM will express the solution of Eq. (1) by the superposition of the basis functions given by Eq. (4) with the unknown coefficients of the basis functions solved by imposing the boundary conditions defined in Eq. (2).

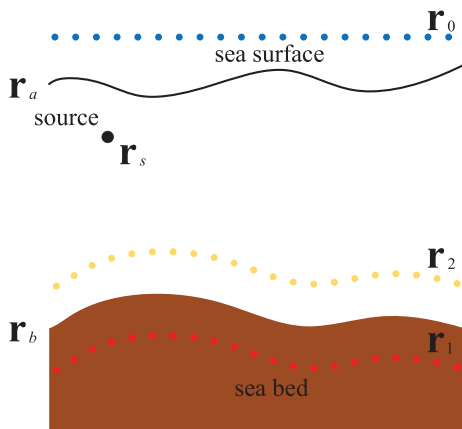


FIG. 1. (Color online) Scheme of the ESM-RPM with the three sets of blue, red, and yellow solid circles above the sea surface, below the seabed, and above the seabed, representing the equivalent sources generating surface reflection, seabed reflection, and transmission, respectively.

To implement the ESM, the field in the waveguide is first separated into four parts: the incident field due to the source, the surface-reflected field $p_{(0)}(\mathbf{r})$, the seabed-reflected field $p_{(1)}(\mathbf{r})$, and the seabed-transmitted field $p_{(2)}(\mathbf{r})$. Then, $p_{(0)}(\mathbf{r})$, $p_{(1)}(\mathbf{r})$, and $p_{(2)}(\mathbf{r})$ can be replaced with fields generated by three sets of equivalent line sources above the sea surface at $\mathbf{r}_{(0)}$ and below and above the seabed at $\mathbf{r}_{(1)}$ and $\mathbf{r}_{(2)}$, respectively, as shown in Fig. 1. Here, the subscripts 0, 1, and 2 specify the positions of the equivalent sources and fields generated by the corresponding sources. Assume that the number of each set of equivalent source is N , $p_{(0,1,2)}(\mathbf{r})$ can be expressed as

$$\begin{cases} p_{(0,1)}(\mathbf{r}) = \sum_{n=1}^N s_{(0,1)n} G^{sp}(\mathbf{r}, \mathbf{r}_{(0,1)n}|k_w), \\ p_{(2)}(\mathbf{r}) = \sum_{n=1}^N s_{(2)n} G^{sp}(\mathbf{r}, \mathbf{r}_{(2)n}|k_s), \end{cases} \quad (5)$$

where the subscript n specifies the n th source placed at $\mathbf{r}_{(0,1,2)}$, and $s_{(0,1,2)n}$ is the strength of the n th source placed at $\mathbf{r}_{(0,1,2)}$. For N field points, Eq. (5) can be expressed as the matrix form

$$\begin{cases} \mathbf{p}_{(0,1)}(\mathbf{r}) = \mathbf{G}^{sp}(\mathbf{r}, \mathbf{r}_{(0,1)}|k_w) \mathbf{s}_{(0,1)}, \\ \mathbf{p}_{(2)}(\mathbf{r}) = \mathbf{G}^{sp}(\mathbf{r}, \mathbf{r}_{(2)}|k_s) \mathbf{s}_{(2)}, \end{cases} \quad (6)$$

where $\mathbf{p}_{(0,1,2)}$ is the $N \times 1$ pressure vector due to the equivalent sources located at $\mathbf{r}_{(0,1,2)}$, $\mathbf{s}_{(0,1,2)}$ is the $N \times 1$ strength vector of the equivalent sources located at $\mathbf{r}_{(0,1,2)}$, and $\mathbf{G}^{sp}(\mathbf{r}, \mathbf{r}_{(0,1)}|k_w)$ and $\mathbf{G}^{sp}(\mathbf{r}, \mathbf{r}_{(2)}|k_s)$ are the $N \times N$ transfer matrices with the entries being $G^{sp}(r_m, \mathbf{r}_{(0,1)n}|k_w)$ and $G^{sp}(r_m, \mathbf{r}_{(2)n}|k_s)$, respectively. Here, r_m is the position of the m th receiver. Similarly, the normal displacement vectors $\mathbf{u}_{(0,1,2)}(\mathbf{r})$, containing N field points as a result of the equivalent sources located at $\mathbf{r}_{(0,1,2)}$, are given by

$$\begin{cases} \mathbf{u}_{(0,1)}(\mathbf{r}) = \mathbf{G}^u(\mathbf{r}, \mathbf{r}_{(0,1)}|k_w) \mathbf{s}_{(0,1)}, \\ \mathbf{u}_{(2)}(\mathbf{r}) = \mathbf{G}^u(\mathbf{r}, \mathbf{r}_{(2)}|k_s) \mathbf{s}_{(2)}. \end{cases} \quad (7)$$

Then, by applying the boundary conditions given by Eq. (2), one can obtain

$$\begin{cases} \mathbf{p}_{\text{inc}}(\mathbf{r}_a) + \mathbf{G}^{sp}(\mathbf{r}_a, \mathbf{r}_{(1)}|k_w) \mathbf{s}_{(1)} = -\mathbf{G}^{sp}(\mathbf{r}_a, \mathbf{r}_{(0)}|k_w) \mathbf{s}_{(0)}, \\ \mathbf{p}_{\text{inc}}(\mathbf{r}_b) + \mathbf{G}^{sp}(\mathbf{r}_b, \mathbf{r}_{(0)}|k_w) \mathbf{s}_{(0)} + \mathbf{G}^{sp}(\mathbf{r}_b, \mathbf{r}_{(1)}|k_w) \mathbf{s}_{(1)} \\ = \mathbf{G}^{sp}(\mathbf{r}_b, \mathbf{r}_{(2)}|k_s) \mathbf{s}_{(2)}, \\ \mathbf{u}_{\text{inc}}(\mathbf{r}_b) + \mathbf{G}^u(\mathbf{r}_b, \mathbf{r}_{(0)}|k_w) \mathbf{s}_{(0)} + \mathbf{G}^u(\mathbf{r}_b, \mathbf{r}_{(1)}|k_w) \mathbf{s}_{(1)} \\ = \mathbf{G}^u(\mathbf{r}_b, \mathbf{r}_{(2)}|k_s) \mathbf{s}_{(2)}, \end{cases} \quad (8)$$

where \mathbf{p}_{inc} and \mathbf{u}_{inc} are the $N \times 1$ incident pressure and normal displacement vectors at the boundaries due to the line source. For iso-velocity water, the incident field resulting from a line source placed at \mathbf{r}_s is given by

$$\mathbf{p}_{\text{inc}}(\mathbf{r}, \mathbf{r}_s) = i\pi H_0^{(1)}(k_w |\mathbf{r} - \mathbf{r}_s|), \quad (9)$$

and $\mathbf{u}_{\text{inc}} = \hat{\mathbf{n}} \nabla \mathbf{p}_{\text{inc}} / \rho_w \omega^2$.

The $N \times 1$ vector of unknown source strengths $\mathbf{s}_{(0,1,2)}$ can be solved by manipulating Eq. (8),

$$\begin{cases} \mathbf{s}_{(0)} = -\mathbf{J} - \mathbf{K}\mathbf{s}_{(1)}, \\ \mathbf{s}_{(1)} = [\mathbf{M}\mathbf{K} - \mathbf{N}]^{-1}[\mathbf{O} - \mathbf{M}\mathbf{J}], \\ \mathbf{s}_{(2)} = \mathbf{R} - \mathbf{Q} - \mathbf{P}\mathbf{s}_{(1)}, \end{cases} \quad (10)$$

where

$$\begin{cases} \mathbf{J} = \mathbf{G}^{sp}(\mathbf{r}_a, \mathbf{r}_{(0)}|k_w)^{-1} \mathbf{p}_{\text{inc}}(\mathbf{r}_a), \\ \mathbf{K} = \mathbf{G}^{sp}(\mathbf{r}_a, \mathbf{r}_{(0)}|k_w)^{-1} \mathbf{G}^{sp}(\mathbf{r}_a, \mathbf{r}_{(1)}|k_w), \\ \mathbf{L} = \mathbf{G}^u(\mathbf{r}_b, \mathbf{r}_{(2)}|k_s) \mathbf{G}^{sp}(\mathbf{r}_b, \mathbf{r}_{(2)}|k_s)^{-1}, \\ \mathbf{M} = \mathbf{L}\mathbf{G}^{sp}(\mathbf{r}_b, \mathbf{r}_{(0)}|k_w) - \mathbf{G}^u(\mathbf{r}_b, \mathbf{r}_{(0)}|k_w), \\ \mathbf{N} = \mathbf{L}\mathbf{G}^{sp}(\mathbf{r}_b, \mathbf{r}_{(1)}|k_w) - \mathbf{G}^u(\mathbf{r}_b, \mathbf{r}_{(1)}|k_w), \\ \mathbf{O} = \mathbf{L}\mathbf{p}_{\text{inc}}(\mathbf{r}_b) - \mathbf{u}_{\text{inc}}(\mathbf{r}_b), \\ \mathbf{P} = \mathbf{G}^{sp}(\mathbf{r}_b, \mathbf{r}_{(2)}|k_s)^{-1} [\mathbf{G}^{sp}(\mathbf{r}_b, \mathbf{r}_{(0)}|k_w) \mathbf{K} \\ \quad - \mathbf{G}^{sp}(\mathbf{r}_b, \mathbf{r}_{(1)}|k_w)], \\ \mathbf{Q} = \mathbf{G}^{sp}(\mathbf{r}_b, \mathbf{r}_{(2)}|k_s)^{-1} \mathbf{G}^{sp}(\mathbf{r}_b, \mathbf{r}_{(0)}|k_w) \mathbf{J}, \\ \mathbf{R} = \mathbf{G}^{sp}(\mathbf{r}_b, \mathbf{r}_{(2)}|k_s)^{-1} \mathbf{p}_{\text{inc}}(\mathbf{r}_b). \end{cases} \quad (11)$$

After solving the source strength vectors, the sound field in the water column and seabed can be calculated using

$$\begin{cases} \mathbf{p}_w(\mathbf{r}) = \mathbf{p}_{\text{inc}}(\mathbf{r}) + \mathbf{G}^{sp}(\mathbf{r}, \mathbf{r}_{(0)}|k_w) \mathbf{s}_{(0)} \\ \quad + \mathbf{G}^{sp}(\mathbf{r}, \mathbf{r}_{(1)}|k_w) \mathbf{s}_{(1)}, \quad \mathbf{r} \in \text{water}, \\ \mathbf{p}_s(\mathbf{r}) = \mathbf{G}^{sp}(\mathbf{r}, \mathbf{r}_{(2)}|k_s) \mathbf{s}_{(2)}, \quad \mathbf{r} \in \text{sediment}. \end{cases} \quad (12)$$

Note that, although the field is first separated into four parts for implementing the ESM-RPM, the surface-reflected and seabed-reflected fields take the multiple interactions with the seabed and sea surface into account, respectively, which means that the ESM-RPM includes the multiple reflections. This is because three equations involving the fields generated by different sets of equivalent sources are coupled into a linear system [Eq. (8)], and then the source strengths are solved globally by satisfying three boundary conditions at the sea surface and water/seabed interface. In addition, Appendix A gives the derivation of the ESM-RPM for the multilayer seabed scenario.

B. Green's function in refractive water using the method of modal projection, incorporating PMLs

In reality, sound propagation is strongly influenced by sound speed variations in shallow water. By replacing the homogeneous free-space Green's function with the refractive free-space Green's function in ESM-RPM, depth-dependent sound speed variations can be taken into account. Here, the method of modal projection is used to incorporate the PML technique for calculating the Green's function in refractive water. As shown in Fig. 2, the starting point is to consider the harmonic acoustic pressure field in the free-

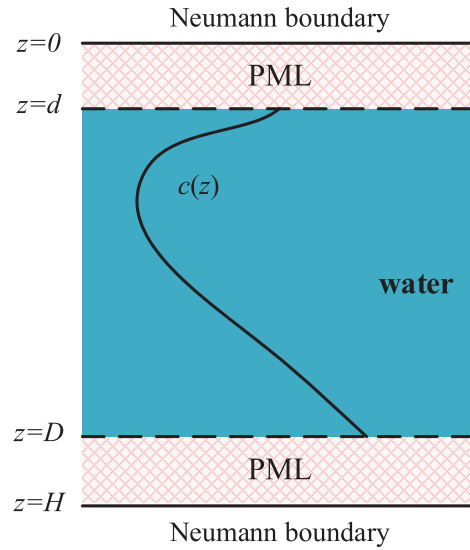


FIG. 2. (Color online) Diagram of the refractive free-space truncated by two PMLs, extending from $z=0$ to $z=d$ and from $z=D$ to $z=H$.

space bounded by a waveguide with two PMLs. The sound speed $c(z)$ in the waveguide is depth dependent, and two Neumann boundary conditions are imposed at $z=0$ and $z=H$. To establish the nonreflecting boundaries, two PMLs extending from $z=0$ to $z=d$ and from $z=D$ to $z=H$ are introduced to the depth-separated wave equation. The PMLs are mathematically equivalent to a stretching of the complex coordinates (Bérenger, 1994); that is,

$$\hat{z} = z + i \int_0^z \delta(\varepsilon) d\varepsilon, \quad (13)$$

where $\delta(\varepsilon)$ is the damping function and ε is the dimensionless coordinate with $\varepsilon = (d - z)/d$ and $\varepsilon = (z - D)/(H - D)$ for the upper and lower PMLs, respectively. Here, first- and second-degree polynomial damping functions (PDF-1 and PDF-2) are considered with mathematical expressions of $\delta(\varepsilon) = \beta\varepsilon$ and $\delta(\varepsilon) = \beta\varepsilon^2$ (Singer and Turkel, 2004; Rabinovich *et al.*, 2010), respectively, where β is a positive real damping coefficient, controlling the rate of damping. From Eq. (13), one can easily obtain that $d\hat{z} = (1 + i\delta(z))dz$. The depth-separated wave equation can then be written as

$$\frac{1}{s(z)} \frac{d}{dz} \left[\frac{1}{s(z)} \frac{d\phi}{dz} \right] + \frac{\omega^2}{c^2(z)} \phi = \kappa^2 \phi, \quad (14)$$

where $s(z) = 1$ for $d < z < D$, $s(z) = 1 + i\delta(z)$, otherwise, and ϕ and κ are the eigenfunction and eigenvalue, respectively. Next, ϕ is projected onto a series of basis functions selected by satisfying the two boundary conditions at $z=0$ and $z=H$,

$$\begin{cases} \phi = \sum_{p=0}^{P-1} v_p \psi_p, \\ \psi_p = \sqrt{\frac{2}{H}} \sin\left(\frac{(p+0.5)\pi z}{H}\right), \end{cases} \quad (15)$$

where P and the subscript p are the total number and the order of basis modes, respectively, and v_p is the projection coefficient. Multiplying both sides of Eq. (14) by ψ_p and then integrating over $0 \leq z \leq H$, the projection yields the following formulation:

$$G + C + B = \kappa^2(E + F), \tag{16}$$

where

$$\left\{ \begin{aligned} B &= \omega^2 \int_0^H s(z) \frac{1}{c^2(z)} \phi \psi_p dz, \\ C &= \frac{d\phi}{dz} \psi_p \Big|_{z=D} - \int_d^D \frac{d\phi}{dz} \frac{d\psi_p}{dz} dz, \\ E &= \int_d^D \phi \psi_p dz, \\ F &= \left[\int_0^d s(z) \phi \psi_p dz + \int_D^H s(z) \phi \psi_p \right] dz, \\ G &= \int_0^d \left[\frac{1}{s(z)} \frac{d^2\phi}{dz^2} - \frac{s'(z)}{s^2(z)} \frac{d\phi}{dz} \right] \psi_p dz \\ &\quad + \int_D^H \left[\frac{1}{s(z)} \frac{d^2\phi}{dz^2} - \frac{s'(z)}{s^2(z)} \frac{d\phi}{dz} \right] \psi_p dz. \end{aligned} \right. \tag{17}$$

In Eq. (17), C and E are analytical, but the remaining integrals need to be treated numerically. Here, G and F represent the PML integrals, and B allows the sound variation because it is numerically integrated with the integrand as a function of the depth-dependent sound speed $c(z)$. The numerical integration scheme for evaluating integrals G , F , and B follows the Clenshaw–Curtis quadrature rules (Waldvogel, 2006), which provide excellent convergence using relatively few depth samplings. Generally, five points per period of the basis mode are sufficient to ensure good convergence. The projection of ϕ_q ($q = 0, 1, \dots, P - 1$) onto ψ_p , defined in Eq. (15), yields the matrix form of Eq. (16),

$$(\mathbf{G} + \mathbf{C} + \mathbf{B})\mathbf{v} = \kappa^2(\mathbf{E} + \mathbf{F})\mathbf{v}, \tag{18}$$

where \mathbf{v} is the projection coefficient matrix.

A generalized matrix eigenvalue problem can then be obtained by left multiplying Eq. (18) by the inverse matrix of $\mathbf{E} + \mathbf{F}$,

$$\mathbf{A}\mathbf{v} = \kappa^2\mathbf{v}, \tag{19}$$

where the matrix $\mathbf{A} = (\mathbf{E} + \mathbf{F})^{-1}(\mathbf{G} + \mathbf{C} + \mathbf{B})$. The eigenvalue κ_q and eigenvector (also known as the projection coefficient vector) for the mode ϕ_q can be easily calculated by solving the eigenvalue decomposition of \mathbf{A} . Finally, the normal mode ϕ_q can be reconstructed using Eq. (15). The Green's functions for sound pressure and normal displacement, which are the fundamental solutions of Eq. (3), can be calculated by a modal sum of ϕ_q (Jensen et al., 2011),

$$\left\{ \begin{aligned} G^{sp}(\mathbf{r}, \mathbf{r}_s | \kappa) &= \frac{1}{2} \sum_{q=0}^{P-1} N_q^2 \phi_q(z_s) \phi_q(z_r) \frac{e^{i\kappa_q x}}{\kappa_q}, \\ G^u(\mathbf{r}, \mathbf{r}_s | \kappa) &= \frac{1}{2\omega^2 \rho} \left[-\chi \frac{dh_b(x)}{dx} \frac{\partial G^{sp}(\mathbf{r}, \mathbf{r}_s | \kappa)}{\partial x} \right. \\ &\quad \left. + \frac{\partial G^{sp}(\mathbf{r}, \mathbf{r}_s | \kappa)}{\partial z} \right], \end{aligned} \right. \tag{20}$$

where $h_b(x)$ is the seabed boundary, $N_q = \sqrt{\int_0^H \phi_q^2 dz}$ is the normalized coefficient, z_s and z_r are the depths of the source and receiver, respectively, $x = |x_s - x_r|$ is the horizontal range, and χ is a factor specifying the sign of the partial derivatives in the x -direction, becoming -1 for $x_r < x_s$, 1 for $x_r > x_s$, and 0 for $x_r = x_s$. The partial derivatives in the above formula can be evaluated easily since the modal sum is depth and range separated. The Green's function, defined in Eq. (20), can be used for both the water and seabed layers with the eigenvalue κ changing accordingly with the sound speed in the layer. Correspondingly, ρ becomes ρ_w in water and ρ_s in the seabed. Note that, to enhance the performance of modal projection method at near-field, the Green's function with a very close source-receiver distance is suggested to be calculated analytically using the sound speed at the depth of the equivalent source. This can be done by replacing the diagonal elements of the matrices that transfer from equivalent sources to their corresponding boundaries (the closest boundaries to the sources) with the analytical solutions, but keeping the non-diagonal elements calculated by modal projection method.

III. RESULTS AND DISCUSSION

Numerical simulations of propagation in shallow water were conducted with an underwater canyon and rough sea surfaces. The seabed boundary $h_b(x)$ of the underwater canyon can be described by

$$h_b(x) = h_0 + \Delta h \exp(-x^2/\gamma^2), \tag{21}$$

where γ was set to $4\Delta h$. The environment parameters of shallow water are defined in Table I.

Initially, the sea surface was assumed to be corrugated surface waves with a wave height function of $h_a(x) = h_s/2 \cos(2\pi x/l)$. Here, h_s and l are the wave height and length, respectively, and take the values shown in the last two rows of Table I. Simulations were first carried out for 2-D across-canyon propagation in both iso-velocity and refractive water under the corrugated surface waves. For the refractive case, the SSP shown in Fig. 3 was used. Then, 3-D along-canyon propagation in both iso-velocity and refractive water under corrugated surface waves was demonstrated using a cosine transform of an assembly of 2-D fields. Further simulations demonstrate both the 2-D across-canyon propagation under 1-D random rough sea surfaces and the 3-D along-canyon propagation under 2-D transversally symmetric random rough sea surfaces.

To implement the ESM-RPM, three sets of equivalent sources were placed at three conformal lines, one above the

TABLE I. Shallow water parameters.

Parameters	Values
Water depth (h_0)	50 m
Canyon depth (Δh)	150 m
Source depth (z_s)	40 m
Water density (ρ_1)	1000 kg/m ³
Water sound speed (c_1)	1500 m/s or SSP shown in Fig. 3
Seabed density (ρ_2)	2000 kg/m ³
Seabed wave speed (c_2)	1800 m/s
Seabed attenuation (α)	0.5 dB/ λ
Surface wave height (h_s)	15 m
Surface wavelength (l)	150 m

sea surface, one below the seabed, and one above the seabed. These were offset from the corresponding boundaries by the same standoff distance. The equivalent sources were distributed at the conformal lines with an element length between two adjacent sources Δ of 0.25λ and a standoff distance d_s of 0.4λ . A detailed discussion of the configuration of the equivalent sources can be found in Appendix B. For the refractive case, Green's functions were evaluated in the domain truncated by the PMLs at depths of one wavelength above $z = -7.5$ m and below $z = 200$ m, respectively. Second-degree polynomial damping functions were used for the PMLs with a damping coefficient β of $5P^{0.25}$ and a PML thickness of 3λ . The determination of the PML parameters is described in Appendix C.

The FE model was adopted here as a benchmark. A full-wave solution of the wavefield provided by the FE model includes all orders of multiple scattering, approaching an exact solution to the Helmholtz equation as the discretization density increases (Isakson and Chotiros, 2011, 2014). For the FE model, triangular meshes were used to discretize both the water and sediment domain with the maximum element size of $1/7$ of the acoustic wavelength. Ten times denser elements were required to the rough sea surface region around the water/seabed interface and source position. The physical domain extending to a maximum depth of $z = 250$ m was truncated by a PML which was composed of a mapping mesh of ten layers with a

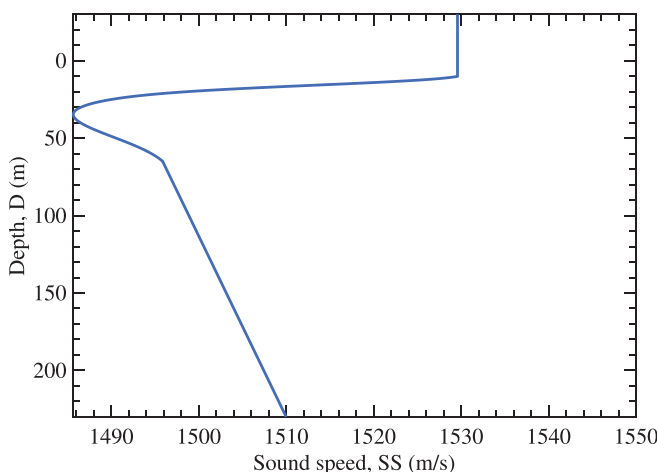


FIG. 3. (Color online) The SSP used in this paper.

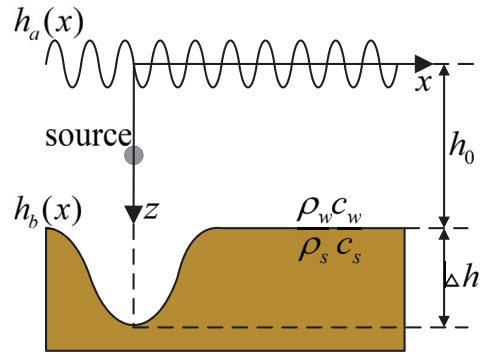


FIG. 4. (Color online) Diagram of the 2-D across-canyon propagation under corrugated surface waves.

thickness of 3λ . Such a meshing scheme can guarantee a convergent FE solution (Isakson and Chotiros, 2011; Qiao et al., 2017; Qing et al., 2019).

A. 2-D range-dependent propagation in iso-velocity shallow water

As shown in Fig. 4, the simulations began with 2-D across-canyon propagation in iso-velocity water under corrugated surface waves. The source was placed at (0 m, 40 m). Here, the transmission loss (TL) is defined by $TL = -20 \log_{10} |p|/|p_0|$, where $|p_0|$ is the pressure at 1-m distance from the source (Jensen et al., 2011). For a monopole source, $|p_0| = 1$. The acoustic impedance at an arbitrary field point is assumed to be the same as that at the source, and changes in impedances across boundaries are neglected to maintain the continuity of the field quantities. First, the ESM-RPM was validated by comparison with the FE model. Excellent agreement with the FE model can be observed in Fig. 5(a) in which the TL is plotted from 1 to 4 km with a receiver depth of 40 m at 50 Hz, thus, demonstrating the accuracy of the proposed ESM-RPM.

Figure 6 shows the 2-D across-canyon propagation. To display the effects of scattering from the corrugated surface waves, the right-hand plot of Fig. 6 illustrates the flat sea surface scenario. Here, scattering is defined as the inhomogeneities of the sea surface (roughnesses) that reradiate the incident sound to both specular and non-specular directions (Bjørnø, 2017). There are significant differences in the fields produced by the two scenarios, especially at propagation ranges above 1.5 km after which the flat surface scenario exhibits greater amplitudes and more apparent mode patterns than does the corrugated surface wave scenario. This can be interpreted as the presence of a rough sea surface promoting the energy transfer from low-order modes to high-order modes (Gao et al., 2017). As the sound propagates across the canyon, higher-order modes continue to be cutoff (become leaky modes) because the water depth decreases. Therefore, the corrugated surface wave scenario leaks more energy in the higher-order modes transformed from the lower-order modes as a result of the presence of the rough surface.

The ESM-RPM enables the separation of the sound field in terms of the incident field and reflected fields from the sea surface and seabed, which aids the analysis of the

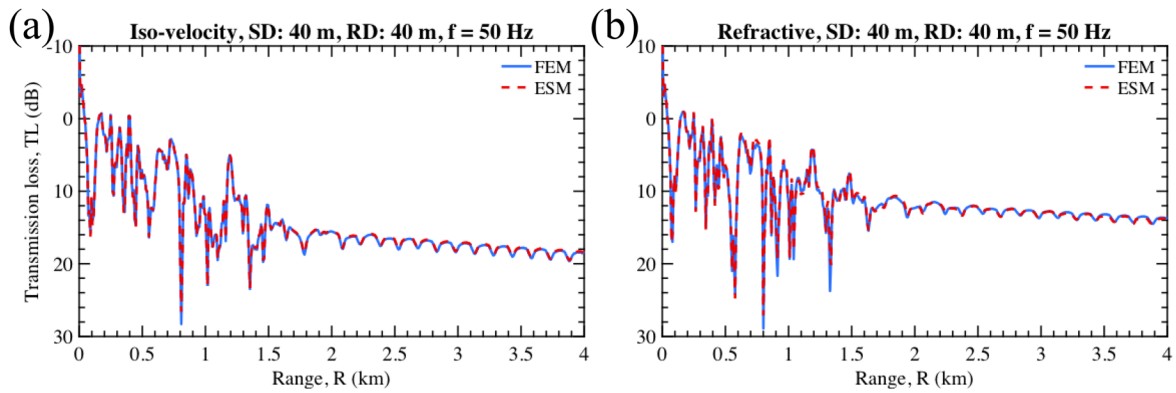


FIG. 5. (Color online) Comparisons of the transmission loss (TL) calculated by the FE model (blue solid line) and the ESM-RPM (red dashed line) for 2-D across-canyon propagation in (a) iso-velocity and (b) refractive water under corrugated surface waves with a receiver depth of 40 m at 50 Hz.

individual scattering contributions from the boundaries for practical applications. Figure 7 plots the fields reflected by the sea surface and seabed in the flat surface and corrugated surface wave scenarios. Here, the reflected fields have been normalized by the incident field, i.e., $|p_0|/|p_{inc}|$ and $|p_1|/|p_{inc}|$. In Fig. 7(a), a caustic pattern can be seen after every crest of the corrugated surface waves, especially in the region around 1 km, where the strongest scattering occurs. In this region, the corrugated surface wave scenario exhibits slightly steeper surface reflection patterns than the flat surface scenario with dominant energies scattered by the sea surface tending to penetrate the seabed at steeper grazing angles. Consequently, weaker seabed reflections are expected in the corresponding regions for the case of corrugated surface waves, which can be observed by comparing Figs. 7(c) and 7(d). Such behaviors coincide with the above analysis of the modal theory and also explain the energy decay at far ranges in the scenario of corrugated surface waves through the increased grazing angle of the surface reflection with respect to the seabed. Note that the interference patterns observed in the surface- and seabed-reflected fields, especially in Fig. 7(b), indicate the presence of multiple reflections.

B. 2-D range-dependent propagation in refractive shallow water

This section considers 2-D across-canyon propagation in water with the SSP shown in Fig. 3 under corrugated

surface waves. Figure 5(b) shows the excellent agreement between the TL calculated by the ESM-RPM and FE model with a receiver depth of 40 m at 50 Hz, hence, validating the ESM-RPM for propagation in refractive water. In comparison with Fig. 6(a), the sound field displayed in Fig. 8(a) for refractive water shows greater amplitudes along the depth axis of 40 m after 1.5 km. The presence of the SSP tends to channel the sound through refraction toward the depth axis of the minimum sound speed. This means that the effects of scattering from the corrugated surface waves become weak as the sound propagates across the canyon. The incident field in refractive water in Fig. 8(b) illustrates that the scattering has been weakened by refraction through the apparent channeling effects along the depth axis of 40 m.

C. 3-D range-dependent propagation in shallow water with translational symmetry

As shown in Fig. 9, this section discusses 3-D along-canyon propagation under 2-D transversally symmetric sea surfaces. Both the depth of the canyon and the 2-D sea surface vary in the same direction. Note that although they are idealized models, sea surfaces with translational symmetry provide a good approximation for situations when the water surface waves have a relatively narrow angular spectrum, meaning that the waves have a large correlation length in the transverse direction. Additionally, the out-of-plane

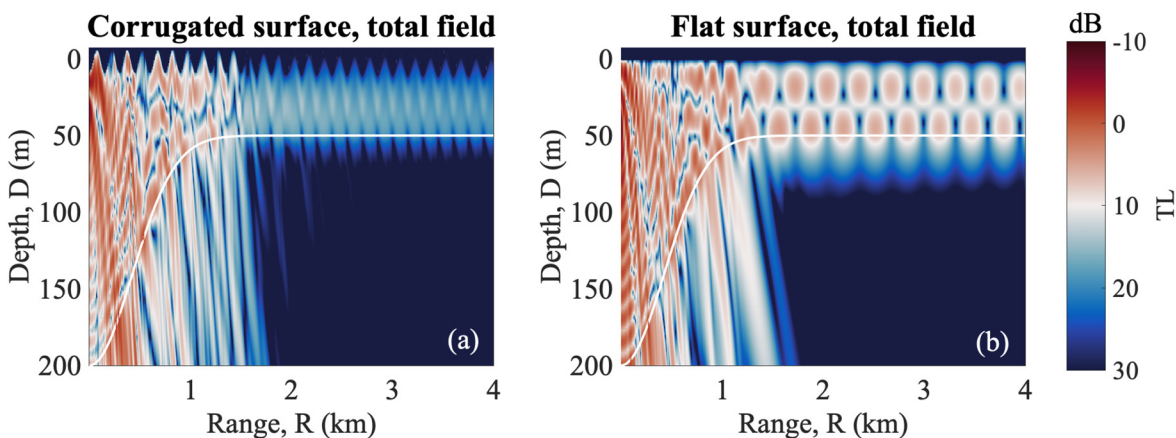


FIG. 6. (Color online) 2-D cross-canyon propagation under (a) corrugated surface waves and (b) a flat sea surface at 50 Hz.

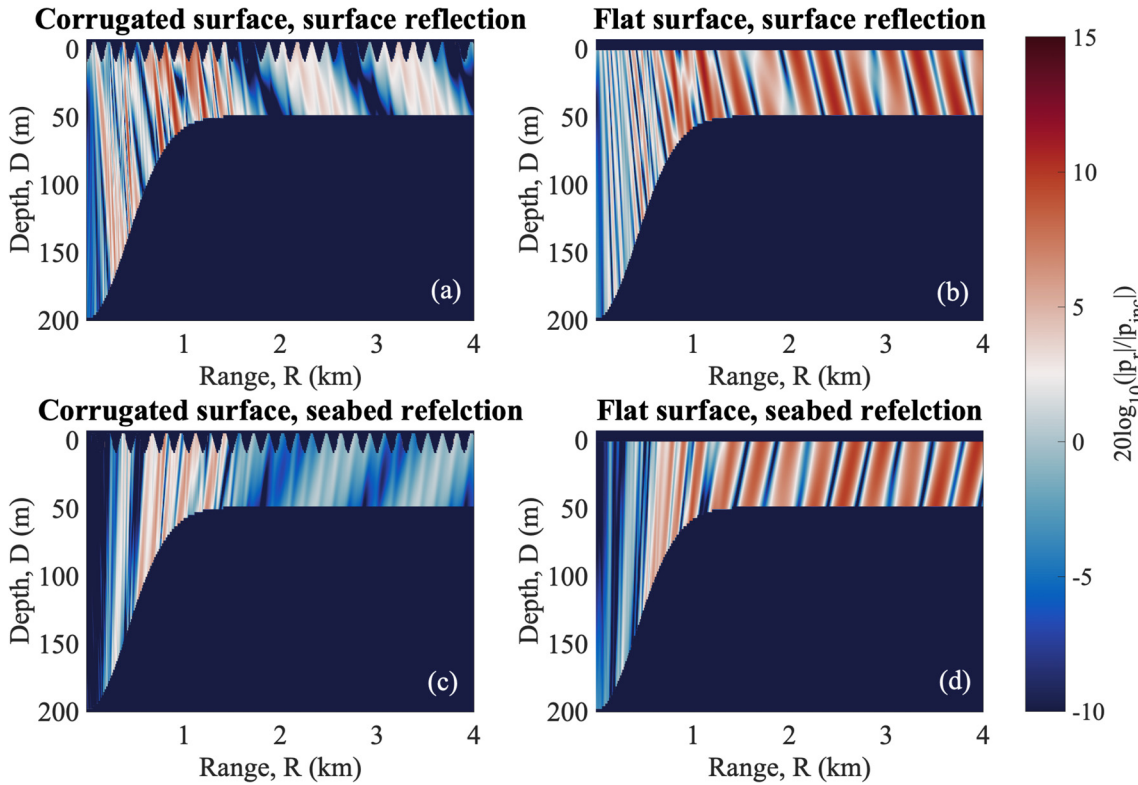


FIG. 7. (Color online) Reflected fields from the sea surface and seabed normalized by the incident field in the 2-D across-canyon plane with the left and right columns displaying the corrugated surface wave and flat surface scenarios, respectively. Here, p_r represents the reflected fields.

scattering and mode-coupling effects are included in the 3-D model. The 3-D sound field was calculated using the cosine transform of an assembly of 2-D fields corresponding to different out-of-plane wavenumbers. When the environment only varies with the x and z axes, the Helmholtz equation governing the 3-D sound field can be reduced to

$$\left[\nabla^2 + (k^2 - k_y^2) \right] p(\mathbf{r}(x, z) | k_y) = 0, \quad (22)$$

with the solution that can synthesise the 3-D solution,

$$p_{3D}(x, y, z) = \int_0^\infty p(\mathbf{r}(x, z) | k_y) \cos(k_y y) dk_y, \quad (23)$$

where k_y is the out-of-plane wavenumber, and the 2-D solution is the transformed field. The above formula is based on the Fourier transform along out-of-plane wavenumbers. The antisymmetric integrand with the sine term vanishes when performing the Fourier transform, which leads to the cosine transform.

For iso-velocity water, each transformed field can be obtained directly by introducing k_y into k_w and k_s in Eq. (4). For refractive water, an additional term $k_y^2 \phi$ should be added to the left-hand side of Eq. (14) with the remaining steps for evaluating the Green's function in refractive water being similar to those presented above. Here, the cosine transform was evaluated using a segmented integration scheme

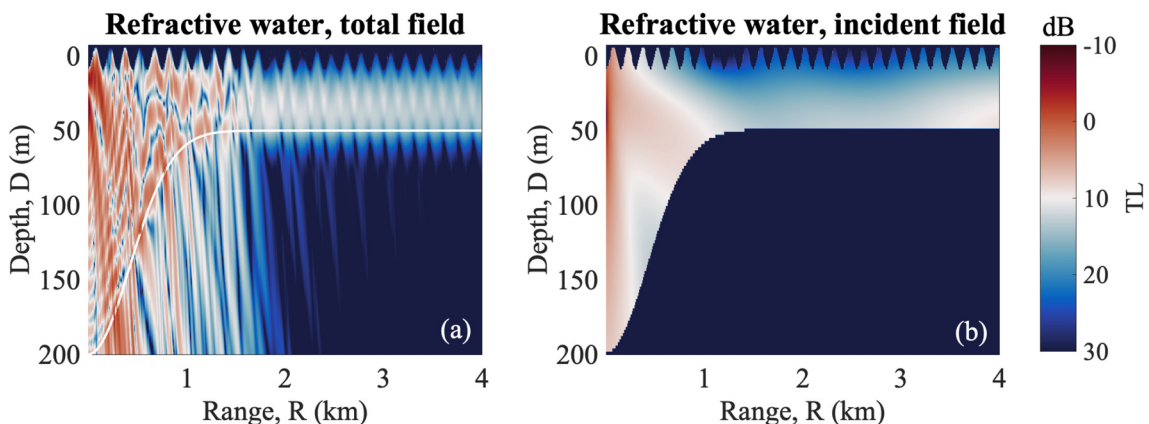


FIG. 8. (Color online) (a) 2-D across-canyon propagation in refractive water with the SSP shown in Fig. 3 under corrugated surface waves at 50 Hz and (b) the corresponding incident field.

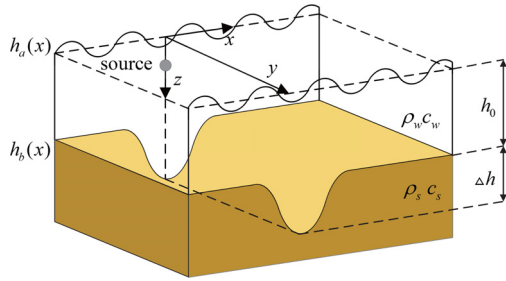


FIG. 9. (Color online) Diagram of a 3-D environment with the underwater canyon and 2-D transversally symmetric sea surfaces.

proposed by He *et al.* (2020). Since the fully 3-D FE model is impractical, a longitudinally invariant finite element (LIFE) model developed by Isakson *et al.* (2014) was used to benchmark the ESM-RPM for the 3-D case. This model is also based on the cosine transform but with each transformed field calculated using the FE model. For both the LIFE model and the ESM-RPM, the segmented integration scheme was performed with 3200 evaluations of 2-D components divided into 8 subintervals. Comparisons with the LIFE model are shown in Fig. 10 in which the TL is plotted as a function of the transverse range y along $x = 800$ m with a receiver depth of 40 m in both iso-velocity and refractive water. Excellent agreements between the two models validate the ESM-RPM for the 3-D scenario.

Figures 11(b) and 11(c) show the 3-D along-canyon propagation in iso-velocity and refractive water in the $z = 40$ m horizontal plane at 50 Hz. The flat surface scenario in iso-velocity water is also shown in Fig. 11(a) for comparison purposes. Focusing effects along the canyon axis are apparent in the flat surface scenario, the result of horizontal refraction and mode-coupling effects. However, in Fig. 11(b), such focusing effects are not as obvious as those in Fig. 11(a) because of the scattering effects. In addition, the “beam-like” patterns around the focusing effects in Fig. 11(b) indicate the out-of-plane scattering from the corrugated surface waves. The sound field in refractive water under corrugated surface waves displayed in Fig. 11(c) exhibits similar scattering features but with greater amplitudes than it does in the iso-velocity case. This is caused by refraction induced by the SSP.

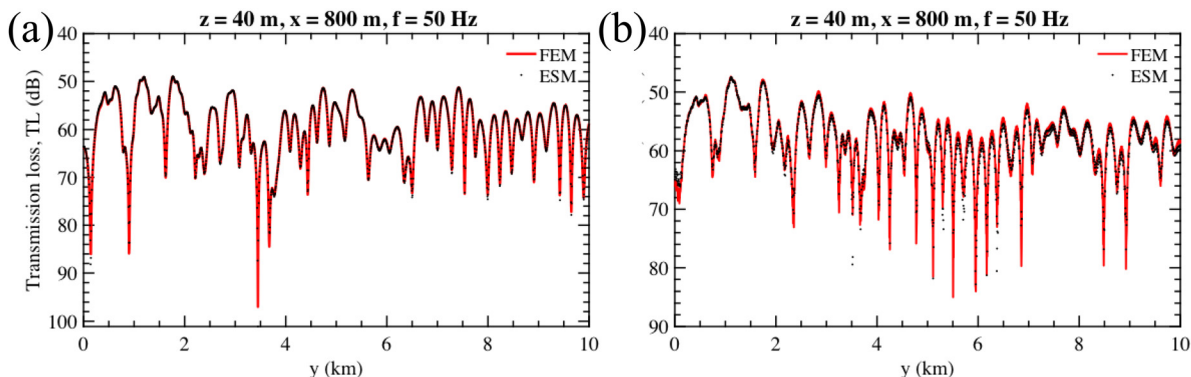


FIG. 10. (Color online) Comparison of the TL along the $x = 800$ m axis calculated by the LIFE model (red solid line) and ESM-RPM (black dots) for 3-D across-canyon propagation in (a) iso-velocity and (b) refractive water under corrugated surface waves with a receiver depth of 40 m at 50 Hz.

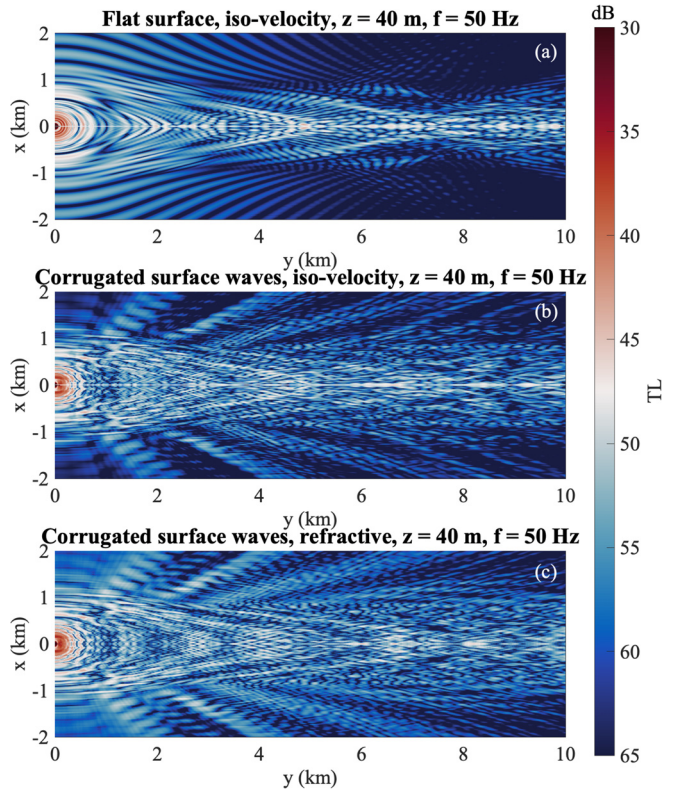


FIG. 11. (Color online) (a) Plot of the flat surface scenario in iso-velocity water. 3-D along-canyon propagation in (b) iso-velocity and (c) refractive water in the $z = 40$ m horizontal plane at 50 Hz.

D. Computation time comparison

This section presents comparisons of the computation time between the FE model and ESM-RPM. In order to make the discretization of the models consistent, the maximum element size of the meshes used in the FE model was reduced to $\lambda/4$ when comparing the computation time (ten times denser meshes are still required for the rough sea surface region around the water/seabed interface and the source position). Comparisons were performed using a laptop with an i9 10900K central processing unit (CPU; Intel Corporation, Santa Clara, CA) with ten cores and 32 GB of random access memory (RAM).

For the 2-D case, it took 48 s to calculate the FE solution, including 36 s for meshing and 12 s for computing. The ESM-RPM only took 0.16 s and 2.8 s to solve the source strength for the iso-velocity and refractive cases, respectively. The sound field at an arbitrary position was then easily obtained. Here, the ESM-RPM shows an enormous advantage in computation time for the iso-velocity case due to the analytical Green's function. Although the ESM-RPM solves the refractive case around 20 times slower than it solves the iso-velocity case, it is still significantly faster than the FE model.

For the 3-D case, the ESM-RPM solves the 3-D sound field by calculating each 2-D transformed field parallelly. The parallel computation was implemented using the *parfor* function in MATLAB. By taking advantage of the inherent high numerical efficiency and parallel computation, the ESM-RPM only took 387 s and 8505 s to finish the calculation for the iso-velocity and refractive cases, respectively, which is much shorter than the 30 120 s taken by the LIFE model to complete the calculation. Moreover, the LIFE model took 80 GB of disk space to store all of the 2-D transformed solutions, whereas the ESM-RPM did not need to save the 2-D solutions.

E. Ensemble averaging study for random rough surfaces

This section examines the case of 2-D across-canyon propagation with 1-D random rough sea surfaces and 3-D

along-canyon propagation with 2-D transversally symmetric random rough sea surfaces. The 1-D Pierson–Moskowitz spectra (Thorsos, 1990) were used to model the wind speed-dependent sea surfaces. The quantities of interest in this section are the average total field (ATF) given by $\langle |p|^2 \rangle$, the coherent field (CF) given by $|\langle p \rangle|^2$, and the average incoherent field (AIF) given by $\langle |p|^2 \rangle - |\langle p \rangle|^2$ (Thorsos *et al.*, 2010). Here, p is the sound pressure from each implementation of the random rough sea surface and $\langle \cdot \rangle$ represents an average over an ensemble of rough sea surface implementations. The ensemble averages were performed with 50 different implementations of the rough surfaces for each wind speed. The CF and AIF represent the specular reflected field and the scattered component of the sound field in the non-specular direction, respectively. The sum of these two terms is the ATF. Generally, stronger scattering can cause larger AIFs but smaller CFs.

First, 2-D across-canyon propagation was considered. To demonstrate significant scattering effects from the sea surface, the wave height should be comparable to the acoustic wavelength (Jackson and Richardson, 2007). For a frequency of 50 Hz, three high wind speeds of 16, 24, and 32 m/s were used, associated with the root mean square (RMS) wave heights of 1.6 m, 3.7 m and 6.1 m. The right column of Fig. 12 shows the ATF in both iso-velocity and refractive water for three different wind speeds with a receiver depth of 40 m at 50 Hz. Overall, both the iso-velocity and refractive water ATFs decrease as the wind becomes stronger with the fluctuations decreasing at the

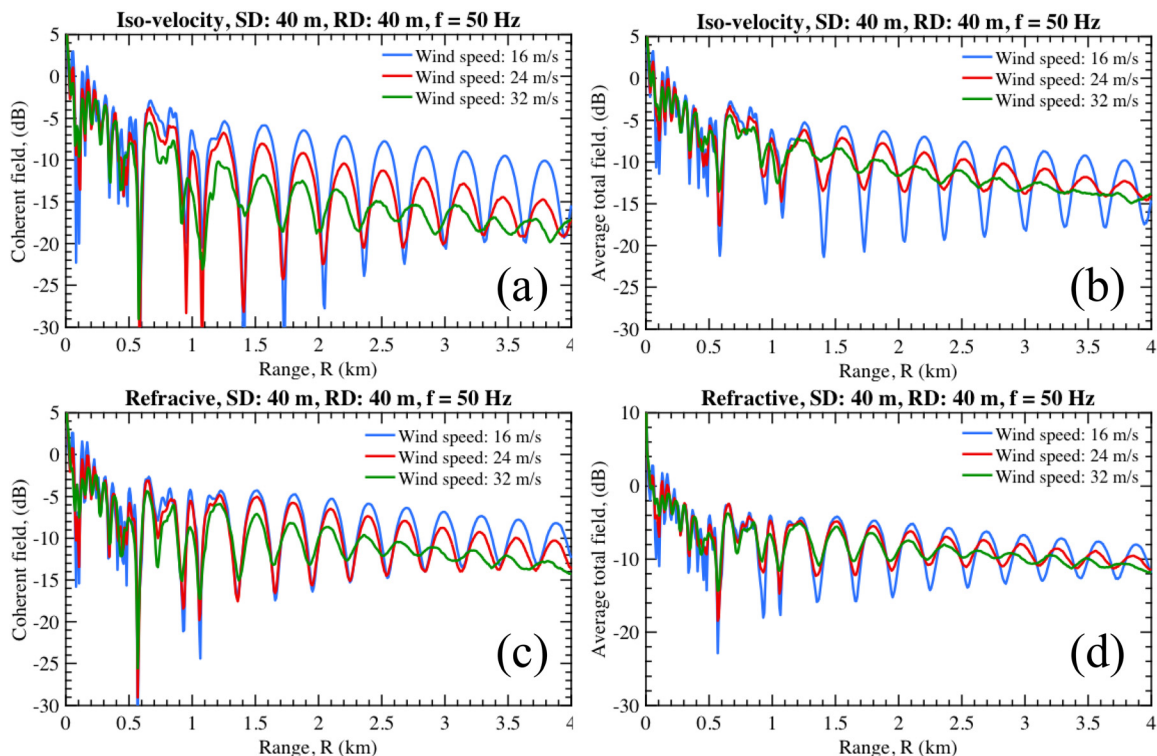


FIG. 12. (Color online) The coherent field (CF) (left column) and ATF (right column) for 2-D across-canyon propagation in (a) and (b) for iso-velocity water and in (c) and (d) for refractive water under 1-D random rough sea surfaces with a receiver depth of 40 m at 50 Hz.

same time. This can be explained by the fact that an increase in wind speed causes the CF, which contains the phase terms of the pressure across different implementations, to decay. The behavior of the CF, declining with the increased wind speed, can be seen in the left column of Fig. 12. Moreover, for each wind speed, the ATF in refractive water exhibits greater overall amplitudes than it does in iso-velocity water. This is because the scattering effects are weakened by refraction.

The results for 3-D along-canyon propagation in iso-velocity water with a wind speed of 32 m/s and a receiver depth of 40 m at 50 Hz are illustrated in Fig. 13. It can be seen that the ATF is slightly smaller and smoother than it is in the flat surface scenario due to the effects of scattering from rough sea surfaces with narrower focusing patterns along the canyon axis. Compared with the flat surface scenario, the CF displays some apparent energy decay along the across-canyon axis but relatively weak energy decay along the canyon axis as a result of the translational symmetry associated with the rough surfaces. In real oceans, the energy decay along the canyon axis would be greater because the sea surfaces are rough in the transversal direction; this will be investigated in detail in future work. Interestingly, the AIF also exhibits apparent focusing patterns along the canyon axis, which may result from the rough scattering involved in the mode coupling across the canyon.

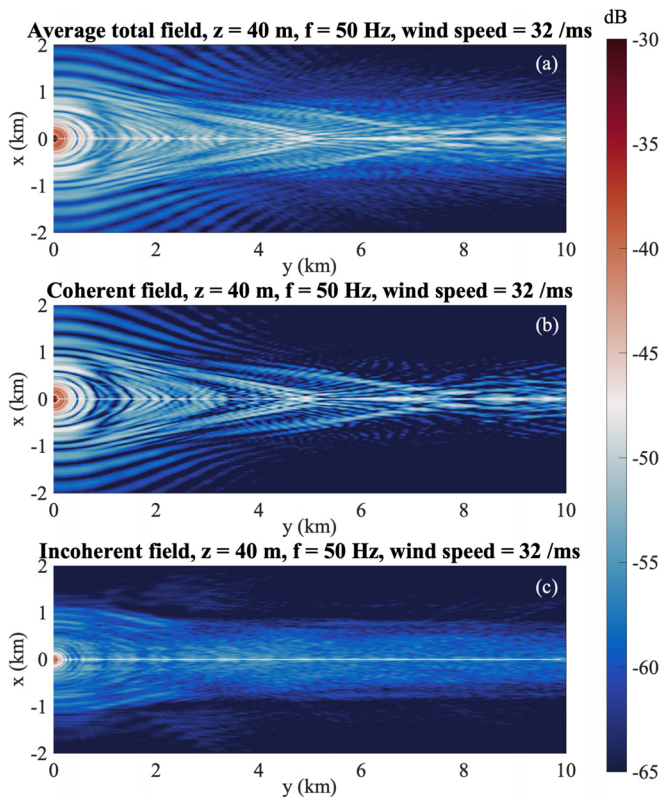


FIG. 13. (Color online) (a) ATF, (b) CF, and (c) AIF in iso-velocity water in the $z = 40$ m horizontal plane at 50 Hz with a wind speed of 32 m/s.

IV. CONCLUSIONS

This paper has presented an ESM-RPM that uses three sets of sources to replace the sea surface-reflected field, seabed-reflected field, and seabed transmitted field. The corresponding strengths of the sources can be obtained by solving the inverse problem based on the boundary conditions at the sea surface and seabed. The propagation in refractive water has been taken into account in the ESM-RPM by evaluating the Green’s function using a modal projection method incorporating the PMLs technique.

Numerical simulations of 2-D across-canyon and 3-D along-canyon propagations were performed for both iso-velocity and refractive shallow water under corrugated surface waves. The ESM-RPM was validated through comparisons with a FE model for both 2-D and 3-D propagation with the results showing that the ESM-RPM agrees closely with the FE model. The sound field separation enabled by the ESM-RPM has been investigated to obtain insights into the scattering effects from the corrugated surface waves and the refraction effects induced by the SSP. The 3-D propagation was demonstrated using a cosine transform to show the effects of out-of-plane scattering. Initial Monte Carlo simulations were performed to demonstrate the versatility of the ESM-RPM in terms of showing the effects of scattering from random rough sea surfaces. The main advantages of the ESM-RPM are that it offers benchmark-quality solutions and achieves high numerical efficiency. It also enables the Monte Carlo simulations required by studies related to boundary scattering to be implemented at a reasonable cost. The proposed model can be applied to the benchmark propagation in shallow water with varying sea surfaces and seabeds or even the modeling of reverberation in shallow water. Besides, the ESM-RPM shows the potential to be used to model time-dependent propagation, for instance, four-dimensional (4-D) propagation under moving sea surfaces, because of its high numerical efficiency. Further work will investigate the extension of the model to a fully 3-D environment.

ACKNOWLEDGMENTS

This work was supported by the National Natural Science Foundation of China under Grant No. 11674075.

APPENDIX A: SOLUTION FOR THE MULTIPLE LAYERS SEABED

The ESM-RPM is extended to the multilayer seabed scenario in this appendix. The multilayer seabed is assumed to be fluid and for the elastic seabed scenario, readers can refer to Abawi and Porter (2007). As shown in Fig. 14, shallow water with a seabed of I layers is considered. Define the sound speed and density of the i th layer of the seabed to be c_{s_i} and ρ_{s_i} ($i = 1, 2, \dots, I$), respectively, and the position of the interface between the i th layer and its upper layer is \mathbf{r}_{b_i} . For the interface at \mathbf{r}_{b_i} , two sets of equivalent sources are placed above and below the interface at $\mathbf{r}_{(2i)}$ and $\mathbf{r}_{(2i-1)}$,

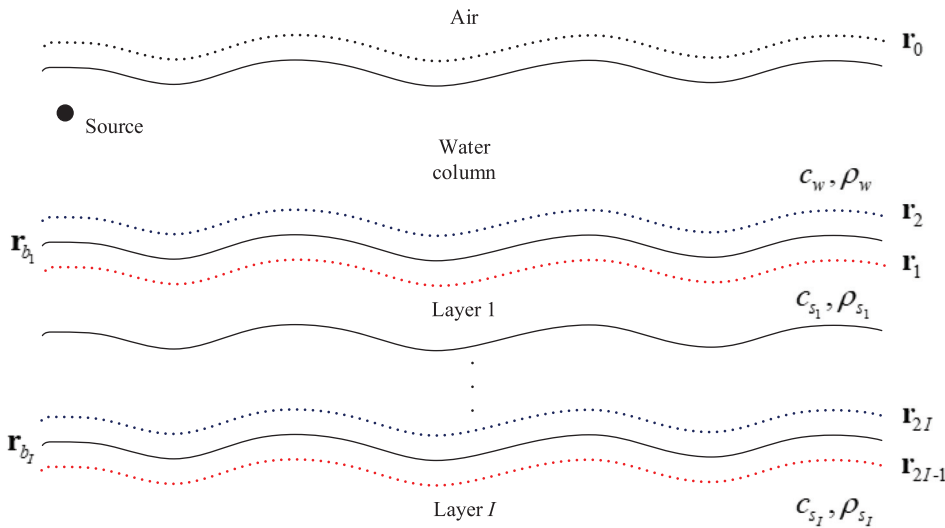


FIG. 14. (Color online) The scheme of the ESM-RPM in the scenario of the multilayer seabed.

respectively, with the sources placed at $\mathbf{r}_{(2i-1)}$ generating the reflected field in the upper layer of the i th layer and those at $\mathbf{r}_{(2i)}$ generating the transmitted field into the i th layer.

Similar to the single-layer seabed scenario, a linear system coupling all fields generated by the $2I + 1$ sets of equivalent sources is given by

$$\begin{cases} \mathbf{G}^{SP}(\mathbf{r}_a, \mathbf{r}_{(0)}|k_w)\mathbf{s}_{(0)} + \mathbf{G}^{SP}(\mathbf{r}_a, \mathbf{r}_{(1)}|k_w)\mathbf{s}_{(1)} = -\mathbf{p}_{inc}(\mathbf{r}_a), \\ \mathbf{G}^{SP}(\mathbf{r}_{b_1}, \mathbf{r}_{(0)}|k_w)\mathbf{s}_{(0)} + \mathbf{G}^{SP}(\mathbf{r}_{b_1}, \mathbf{r}_{(1)}|k_w)\mathbf{s}_{(1)} - \mathbf{G}^{SP}(\mathbf{r}_{b_1}, \mathbf{r}_{(2)}|k_{s_1})\mathbf{s}_{(2)} = -\mathbf{p}_{inc}(\mathbf{r}_{b_1}), \\ \mathbf{G}^U(\mathbf{r}_{b_1}, \mathbf{r}_{(0)}|k_w)\mathbf{s}_{(0)} + \mathbf{G}^U(\mathbf{r}_{b_1}, \mathbf{r}_{(1)}|k_w)\mathbf{s}_{(1)} - \mathbf{G}^U(\mathbf{r}_{b_1}, \mathbf{r}_{(2)}|k_{s_1})\mathbf{s}_{(2)} = -\mathbf{u}_{inc}(\mathbf{r}_{b_1}), \\ \vdots \\ \mathbf{G}^{SP}(\mathbf{r}_{b_i}, \mathbf{r}_{(2i-2)}|k_{s_{i-1}})\mathbf{s}_{(2i-2)} + \mathbf{G}^{SP}(\mathbf{r}_{b_i}, \mathbf{r}_{(2i-1)}|k_{s_{i-1}})\mathbf{s}_{(2i-1)} - \mathbf{G}^{SP}(\mathbf{r}_{b_i}, \mathbf{r}_{(2i)}|k_{s_i})\mathbf{s}_{(2i)} = 0, \\ \mathbf{G}^U(\mathbf{r}_{b_i}, \mathbf{r}_{(2i-2)}|k_{s_{i-1}})\mathbf{s}_{(2i-2)} + \mathbf{G}^U(\mathbf{r}_{b_i}, \mathbf{r}_{(2i-1)}|k_{s_{i-1}})\mathbf{s}_{(2i-1)} - \mathbf{G}^U(\mathbf{r}_{b_i}, \mathbf{r}_{(2i)}|k_{s_i})\mathbf{s}_{(2i)} = 0, \end{cases} \quad (A1)$$

where the subscript $i = 0, 1, \dots, I$ represents the number of seabed layers. The above linear system can be expressed as $[A]\{x\} = \{b\}$, which can be solved using either the

Gaussian elimination or the iterative method. Then, the field in the water column can be calculated in a way similar to that presented in Eq. (12), and the field in each layer of the

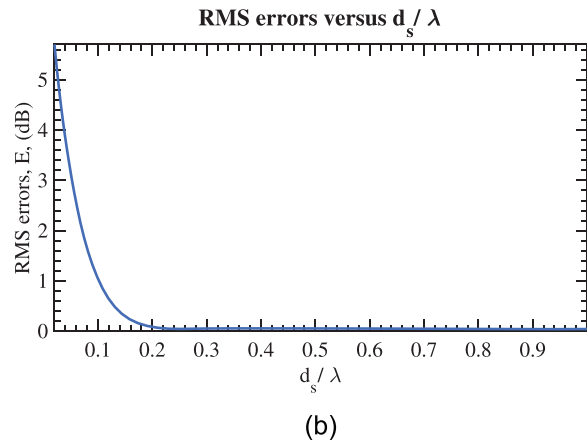
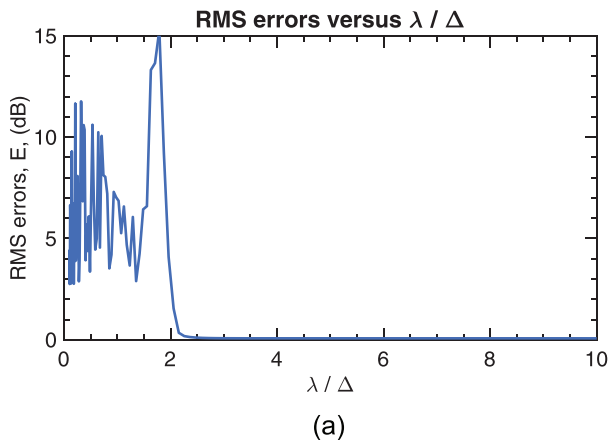


FIG. 15. (Color online) The RMS error as a function of (a) the ratio of the acoustic wavelength λ to the element length Δ between adjacent equivalent sources along the conformal surface, and (b) the ratio of the standoff distance d_s to the acoustic wavelength λ , calculated using the pressure along the same line shown in that section. Here, $d_s = 0.4\lambda$ for (a) and $\Delta = 0.25\lambda$ for (b).

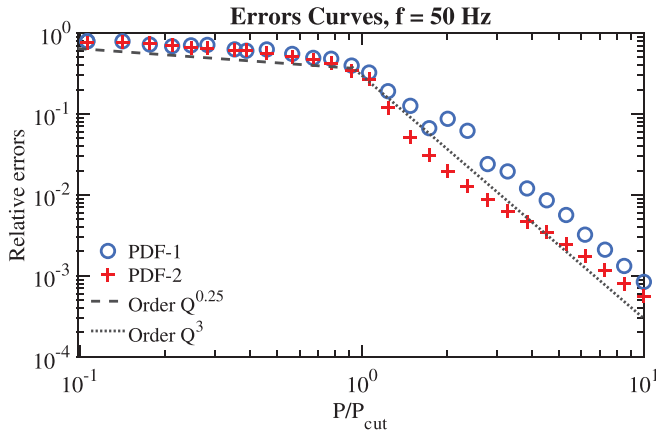


FIG. 16. (Color online) Relative error curve as a function of P/P_{cut} at 50 Hz.

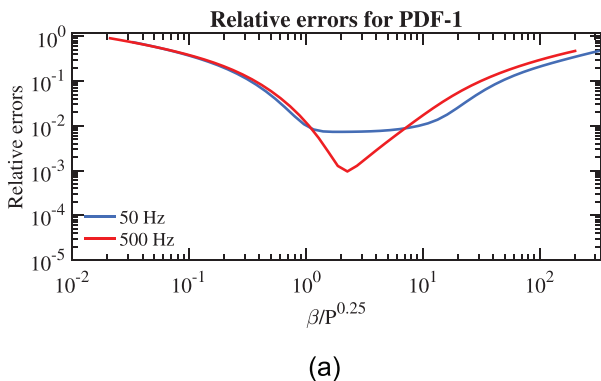
seabed can be reconstructed by superposing the corresponding reflected and transmitted fields after solving the linear system.

APPENDIX B: DETERMINATION OF THE CONFIGURATION OF EQUIVALENT SOURCES

The influence of the configuration of equivalent sources is discussed in this appendix. The RMS error E (in dB) over the propagation range is defined as

$$E = \frac{1}{M} \sum_{m=1}^M \left| 10 \log_{10} \left\{ \left| \frac{p}{p_{ref}} \right| \right\} \right|, \tag{B1}$$

where p_{ref} and p are the sound pressures calculated using the FE model and the ESM-PRM, respectively, along the same line shown in Fig. 5(a). E is plotted as a function of the ratio of the acoustic wavelength λ to the element length Δ between adjacent equivalent sources along the conformal surface in Fig. 15(a), remaining large when Δ is greater than $\lambda/2$ but shrinking rapidly thereafter. This behavior coincides with an equivalent of the Nyquist criterion for sampling waveforms, suggesting that the distribution of equivalent sources requires at least approximately 2.5 points per wavelength.



(a)

The influence of the standoff distance d_s can be studied by calculating E as a function of the ratio of d_s to λ . The error shown in Fig. 15(b) decreases significantly as d_s increases, eventually remaining lower than 0.1 dB when $d_s > 0.2\lambda$. The large errors for small d_s are induced by the rise in the singularity of the normal displacement transfer matrix.

Based on these results, the following configuration of equivalent sources is recommended: a conformal line to the corresponding boundary with an element length Δ of 0.25λ and a standoff distance d_s of 0.4λ .

APPENDIX C: PARAMETER SELECTION FOR THE PMLS

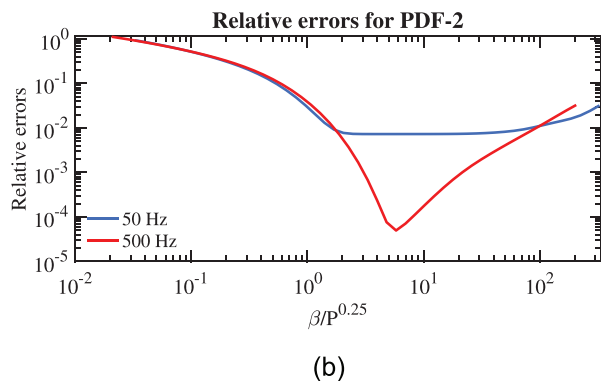
This appendix discusses the determination of the PML parameters, including the PML thicknesses and damping function, by assessing the relative errors with respect to a reference solution. The Green’s function in a homogeneous free-space is taken as the reference solution. This can be written analytically as

$$G_{analy}(x, z) = \frac{i}{4\pi} H_0^{(1)} \left(k \sqrt{(x - x_0)^2 + (z - z_0)^2} \right), \tag{C1}$$

where (x_0, z_0) is the position of the line source. The relative errors are given by

$$Errors = \frac{\left(\int_{\Omega} |G_{analy} - G|^2 dx dz \right)^{1/2}}{\left(\int_{\Omega} |G_{analy}|^2 dx dz \right)^{1/2}}, \tag{C2}$$

where G is the solution calculated by the proposed method, and Ω is the calculation domain. In this case, Ω is truncated by two PMLs at depths of -30 and 230 m, ranging from 1 to 4 km with a sound speed of 1500 m/s. The source was placed at a depth of $z_0 = 100$ m, and $x_0 = 0$. The PML thickness d and β were set to default values of 3λ and $20P^{0.25}$, respectively, unless specified. The parameter selection for d and β will be discussed further in the following simulations.



(b)

FIG. 17. (Color online) Relative errors as a function of $\beta/P^{0.25}$ for the PMLs using polynomial damping functions of degrees one (left column) and two (right column) with a PML thickness of 3λ at 50 Hz (blue solid line) and 500 Hz (red solid line).

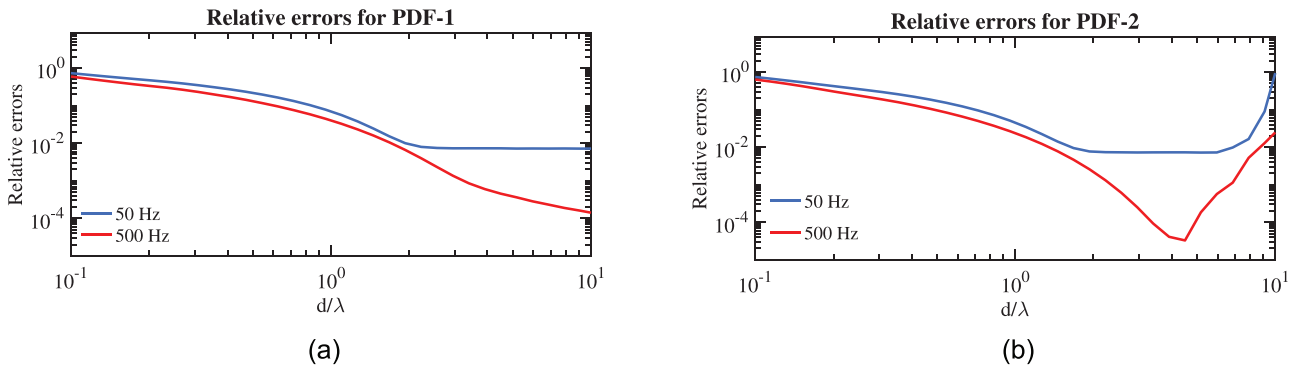


FIG. 18. (Color online) Relative errors as a function of d/λ for the PMLs using polynomial damping functions of degree one (left column) and two (right column) with $\beta = 2.5P^{0.25}$ and $\beta = 5P^{0.25}$ at 50 Hz and 500 Hz, respectively.

First, the number of basis modes P was determined by analyzing the convergence of the relative errors. Figure 16 shows the relative errors as a function of the ratio of P to the number of cutoff basis modes P_{cut} ($P_{\text{cut}} = 2Hf/c$), using the two types of damping functions at 50 Hz. The relative errors for both damping functions steadily decrease according to $1/P^{0.25}$ when $P < P_{\text{cut}}$ after which they decay more rapidly according to $1/P^3$. The modal projection method truncates the free-space with two PMLs to calculate the free-field Green's function, which can be considered as the continuous spectrum. Basis modes containing only propagating modes can provide sufficient convergence for a bounded space where the field can be expressed as the discrete spectrum. When dealing with the free-field truncated by PMLs, the propagating modes (discrete spectrum) are insufficient, and the evanescent modes must be taken into account to approximate the continuous spectrum accurately. Besides, the attenuating behavior of the evanescent modes coincides with the absorption of the reflection from outer boundaries. Therefore, a rise of evanescent modes can accelerate the convergence after $P > P_{\text{cut}}$. Although an increasing P results in higher accuracy, there is some additional numerical cost. $P = 3P_{\text{cut}}$ provides sufficient accuracy with errors barely exceeding 1% and, therefore, this value was used in the subsequent simulations.

To further determine the optimal damping function and the corresponding β , Fig. 17 presents the relative errors as a

function of $\beta/P^{0.25}$ for the two types of damping functions at two different frequencies. Initially, the errors decrease as β increases for both PDF-1 and PDF-2, which coincides with the polynomial damping functions eliminating the spurious reflections from the outer boundary of the PMLs by enlarging the damping coefficients (Bermúdez *et al.*, 2007). After reaching their minima, the errors at 50 Hz tend to remain stable and then steadily rebound, whereas the errors at 500 Hz suddenly rise as β increases. This rebound in the errors can be interpreted as an excessively complex stretching induced by large damping coefficients. Note that the minimum error at 500 Hz for PDF-2 is significantly smaller than the minimum error for PDF-1. Additionally, PDF-2 displays a wider β range over which the errors are less than 1%. This indicates that PDF-1 is more sensitive to the damping coefficient. The above analysis suggests that robust results can be obtained using PDF-1 with $\beta = 2.5P^{0.25}$ and PDF-2 with $\beta = 5P^{0.25}$ for both the low and high frequencies.

Next, the errors are plotted as a function of the PML thicknesses divided by the acoustic wavelength in Fig. 18. The errors for PDF-1 decrease as the PMLs become thicker. PDF-2 exhibits a similar trend initially but starts to increase after d exceeds 3λ in the 50 Hz case and 5λ in the 500 Hz case. The results show that sufficient accuracy can be obtained using PMLs with $d = 3\lambda$ in both cases.

The above results suggest that the optimal PML setup is PDF-2 with $\beta = 5P^{0.25}$ and a PML thickness of 3λ . This PML setup was used for propagation in refractive water in this study. Using this optimal PML setup, the real part of the sound pressure in Ω truncated at 1 km is as shown in Fig. 19. No reflection from outer boundaries of the waveguide can be seen, thus, demonstrating the effectiveness of the PMLs.

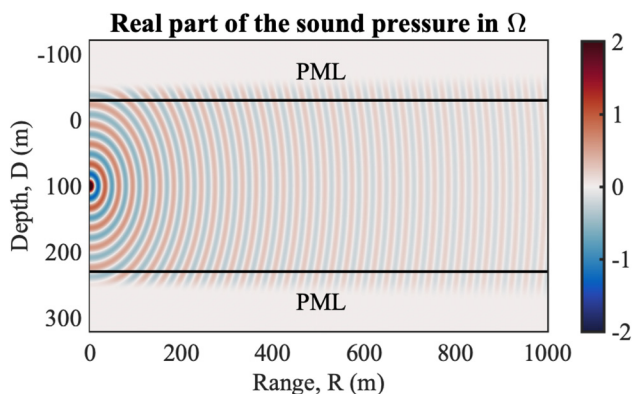


FIG. 19. (Color online) The real part of the sound pressure in Ω , calculated using the optimal PML setup.

Abawi, A. T., and Porter, M. B. (2007). "Propagation in an elastic wedge using the virtual source technique," *J. Acoust. Soc. Am.* **121**(3), 1374–1382.

Ballard, M. S. (2013). "Three-dimensional acoustic propagation under a rough sea surface," *Proc. Mtgs. Acoust.* **19**, 070077.

Ballard, M. S., Goldsberry, B. M., and Isakson, M. J. (2015). "Normal mode analysis of three-dimensional propagation over a small-slope cosine shaped hill," *J. Comput. Acoust.* **23**(03), 1550005.

Bérenger, J.-P. (1994). "A perfectly matched layer for the absorption of electromagnetic waves," *J. Comput. Phys.* **114**(2), 185–200.

- Bermúdez, A., Hervella-Nieto, L., Prieto, A., and Rodríguez, R. (2007). "An optimal perfectly matched layer with unbounded absorbing function for time-harmonic acoustic scattering problems," *J. Comput. Phys.* **223**(2), 469–488.
- Bjørnø, L. (2017). *Applied Underwater Acoustics* (Elsevier, Amsterdam), Chap. 5.
- Bottero, A., Cristini, P., Komatitsch, D., and Asch, M. (2016). "An axisymmetric time-domain spectral-element method for full-wave simulations: Application to ocean acoustics," *J. Acoust. Soc. Am.* **140**(5), 3520–3530.
- Bottero, A., Cristini, P., Komatitsch, D., and Brissaud, Q. (2018). "Broadband transmission losses and time dispersion maps from time-domain numerical simulations in ocean acoustics," *J. Acoust. Soc. Am.* **144**(3), EL222–EL228.
- Collins, M. D. (1989). "Applications and time-domain solution of higher-order parabolic equations in underwater acoustics," *J. Acoust. Soc. Am.* **86**(3), 1097–1102.
- Collins, M. D. (1993). "A split-step Padé solution for the parabolic equation method," *J. Acoust. Soc. Am.* **93**(4), 1736–1742.
- Cristini, P., and Komatitsch, D. (2012). "Some illustrative examples of the use of a spectral-element method in ocean acoustics," *J. Acoust. Soc. Am.* **131**(3), EL229–EL235.
- DiNapoli, F. R., and Deavenport, R. L. (1980). "Theoretical and numerical Green's function field solution in a plane multilayered medium," *J. Acoust. Soc. Am.* **67**(1), 92–105.
- Evans, R. B. (1983). "A coupled mode solution for acoustic propagation in a waveguide with stepwise depth variations of a penetrable bottom," *J. Acoust. Soc. Am.* **74**(1), 188–195.
- Fawcett, J. A. (1992). "A derivation of the differential equations of coupled-mode propagation," *J. Acoust. Soc. Am.* **92**(1), 290–295.
- Gao, B., Wang, N., and Wang, H. Z. (2017). "Investigation of sea surface effect on shallow water reverberation by coupled mode method," *J. Comput. Acoust.* **25**(02), 1750017.
- He, T., Humphrey, V. F., Mo, S., and Fang, E. (2020). "Three-dimensional sound scattering from transversely symmetric surface waves in deep and shallow water using the equivalent source method," *J. Acoust. Soc. Am.* **148**(1), 73–84.
- Isakson, M. J., and Chotiros, N. P. (2011). "Finite element modeling of reverberation and transmission loss in shallow water waveguides with rough boundaries," *J. Acoust. Soc. Am.* **129**(3), 1273–1279.
- Isakson, M. J., and Chotiros, N. P. (2014). "Finite element modeling of acoustic scattering from fluid and elastic rough interfaces," *IEEE J. Ocean. Eng.* **40**(2), 475–484.
- Isakson, M. J., Goldsberry, B., and Chotiros, N. P. (2014). "A three-dimensional, longitudinally-invariant finite element model for acoustic propagation in shallow water waveguides," *J. Acoust. Soc. Am.* **136**(3), EL206–EL211.
- Jackson, D., and Richardson, M. (2007). *High-Frequency Seafloor Acoustics* (Springer Science and Business Media, New York), p. 173.
- Jensen, F. B., Kuperman, W. A., Porter, M. B., and Schmidt, H. (2011). *Computational Ocean Acoustics* (Springer Science and Business Media, New York).
- Koopmann, G. H., Song, L., and Fahline, J. B. (1989). "A method for computing acoustic fields based on the principle of wave superposition," *J. Acoust. Soc. Am.* **86**(6), 2433–2438.
- Lin, Y.-T., Duda, T. F., and Newhall, A. E. (2013). "Three-dimensional sound propagation models using the parabolic-equation approximation and the split-step Fourier method," *J. Comput. Acoust.* **21**(01), 1250018.
- McDonald, B. E. (1996). "Bathymetric and volumetric contributions to ocean acoustic mode coupling," *J. Acoust. Soc. Am.* **100**(1), 219–224.
- Pekeris, C. L. (1948). "Theory of propagation of explosive sound in shallow water," available at https://www.google.com/books/edition/Theory_of_Propagation_of_Explosive_Sound/JP0IAQAIAAJ?hl=en&gbpv=1&dq=Theory+of+propagation+of+explosive+sound+in+shallow+water&printsec=frontcover#spf=1611754027928.
- Qiao, G., Qing, X., Feng, W., Liu, S., Nie, D., and Zhang, Y. (2017). "Elastic feature of cylindrical shells extraction in time-frequency domain using biomimetic dolphin click," *J. Acoust. Soc. Am.* **142**(6), 3787–3795.
- Qing, X., White, P. R., Leighton, T. G., Liu, S., Qiao, G., and Zhang, Y. (2019). "Three-dimensional finite element simulation of acoustic propagation in spiral bubble net of humpback whale," *J. Acoust. Soc. Am.* **146**(3), 1982–1995.
- Rabinovich, D., Givoli, D., and Bécache, E. (2010). "Comparison of high-order absorbing boundary conditions and perfectly matched layers in the frequency domain," *Int. J. Numer. Methods Biomed. Eng.* **26**(10), 1351–1369.
- Simon, B., Isakson, M., and Ballard, M. (2018). "Modeling acoustic wave propagation and reverberation in an ice covered environment using finite element analysis," *Proc. Mtgs. Acoust.* **33**, 070002.
- Singer, I., and Turkel, E. (2004). "A perfectly matched layer for the Helmholtz equation in a semi-infinite strip," *J. Comput. Phys.* **201**(2), 439–465.
- Sturm, F. (2016). "Leading-order cross term correction of three-dimensional parabolic equation models," *J. Acoust. Soc. Am.* **139**(1), 263–270.
- Tappert, F. D. (1977). "The parabolic approximation method," in *Wave Propagation and Underwater Acoustics* (Springer, Berlin, Heidelberg), pp. 224–287.
- Thorsos, E. I. (1990). "Acoustic scattering from a 'Pierson–Moskowitz' sea surface," *J. Acoust. Soc. Am.* **88**(1), 335–349.
- Thorsos, E. I., Henryey, F. S., Elam, W. T., Hefner, B. T., Reynolds, S. A., and Yang, J. (2010). "Transport theory for shallow water propagation with rough boundaries," *AIP Conf. Proc.* **1272**, 99–105.
- Waldvogel, J. (2006). "Fast construction of the Fejér and Clenshaw–Curtis quadrature rules," *BIT Numer. Math.* **46**(1), 195–202.